Exploring 0D lead-free metal halide with highly efficient blue light emission and high-sensitivity photodetection†

Yu-Yin Wang,[a] Huai-Yuan Kang,[a] Shao-Ya Zhang,[a] Hao Qu,[a] Lin Zhu,[a] Dan Zhao,[a] Xian-Feng Li,*[b] Xiao-Wu Lei[a] and Cheng-Yang Yue*[a]

Environmentally friendly and highly efficient blue luminescent materials are an unremitting pursuit in the optoelectronic field. Herein, we assembled a new 0D lead-free metal halide of (F-PPA)ZnBr$_4$, which exhibits narrow blue light emission with a remarkable PLQY of 50.15%, high stability and high detection sensitivity toward UV light. These results indicate the potential for the application of low-dimensional zinc-based halides in multiple optoelectronic devices.

Organic–inorganic halide perovskites have become increasingly popular over the past decade because of their inherently fascinating properties, such as unique defect tolerance, high carrier mobility, and size-varying optical properties, resulting in various applications in the fields of solar photovoltaic cells, light-emitting diodes, lasers, photodetectors and ferroelectrics, *etc.*[1–4] Organic–inorganic metal halides are expected to become emerging luminescent materials as candidates of perovskites for realizing high-performance optoelectronic applications.[5–10] Among all the photoluminescence (PL) qualities, PL quantum yield (PLQY) is one of the most important indicators for optoelectronic applications of hybrid halide perovskites. Therefore, it is crucial to reach high photoluminescence quantum yields (PLQYs) for luminescent perovskite materials, especially in the blue light spectral range.

Among the luminescent organic–inorganic metal halides (OIMHs) of various dimensions, the excellent luminescent characteristics of three-dimensional (3D) perovskites are primarily favoured by researchers due to high PLQY in the green and red spectral range. However, blue emissive perovskite remains subject to low PLQY, and substantial structural modification strategies were adopted to improve the emission efficiency of blue emissive perovskites. Many studies have shown that a reduction in their dimensions will significantly enhance the luminescent performance. Among organic–inorganic hybrid perovskites, zero-dimensional (0D) halide perovskites can obtain higher PLQYs than 3D perovskites due to their larger exciton binding energy.[11–15] The higher PLQYs occur because 0D OIMHs have spatially isolated metal halide polyhedral units, which avoid electronic interactions between adjacent polyhedrons. There is no doubt that 0D OIMHs are the best choice as luminescent materials with high PLQYs for optoelectronic applications. One of the typical representative cases is 0D OIMH of $(C_9NH_{20})_7(PbCl_4)Pb_3Cl_{11}$, which has a high PLQY of 83% in the blue light emission range due to the rapid excited state structural reorganization of the $[Pb_3Cl_{11}]^{5-}$ cluster.

On the other hand, the application of organic–inorganic metal halide photodetectors is receiving increasing attention due to the growing demand for wireless sensor networks, especially for monitoring human exposure to UV light.[16–20] This is of great significance to prevent skin cancer and accelerated aging due to excessive exposure to ultraviolet rays. Meanwhile, humans' moderate exposure to UV light from the sun also has positive health effects, that is, the moderate exposure of the skin to UV radiation triggers the synthesis of vitamin D and negatively affects certain pathogens. Additionally, an excellent organic–inorganic metal halide photodetector also needs to exhibit a linear correlation between optical power and photocurrent, and avoid background radiation (visible and infrared) from obscuring the UV signal, thereby significantly suppressing the influence of visible light.[21] Therefore, there is an urgent need to develop a new luminescent material with optoelectronic properties that is environmentally friendly, has high PLQYs and high stability, and has high detection sensitivity toward UV light.

Herein, we successfully synthesized a lead-free example of 0D OIMH **(F-PPA)ZnBr$_4$** (**F-PPA** = $C_{10}H_{14}FN_2$:1-(2-fluorophenyl)-piperazine), and utilized its inherent large band gap to achieve

[a] *School of Chemistry, Chemical Engineer and Materials, Jining University, Qufu, Shandong, 273155, P. R. China. E-mail: yuechengyang@126.com*
[b] *Institute of Nanotechnology (INT), Karlsruhe Institute of Technology (KIT), Hermann-von-Helmholtz Platz 1, 76344 Eggenstein-Leopoldshafen, Germany. E-mail: xianfeng.li@kit.edu*

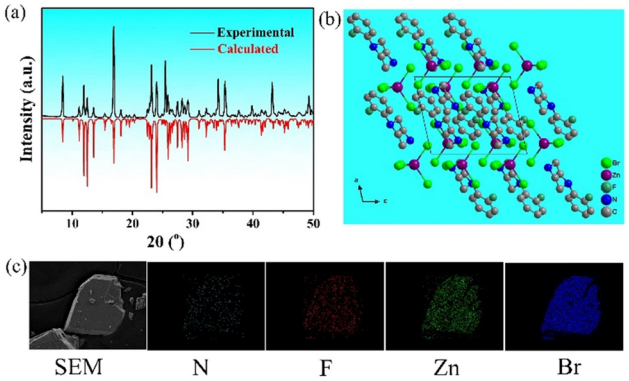

Fig. 1 (a) Experimental and simulated PXRD patterns of **(F-PPA)ZnBr$_4$** powder at 298 K. (b) Packing crystal structure. (c) Representative SEM image of a block-shaped single crystal and corresponding elemental distribution of F, Zn, Br, and N.

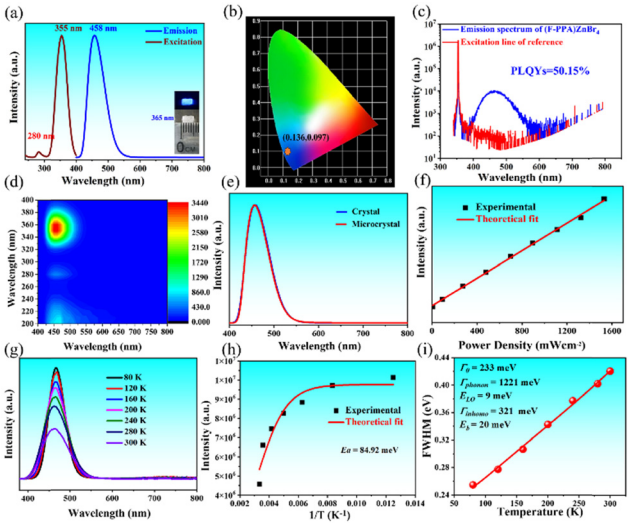

Fig. 2 Systematic PL characterizations of **(F-PPA)ZnBr$_4$**: (a) PL excitation and emission spectra; (b) CIE chromaticity coordinates; (c) the PLQY of the compound; (d) the 3D consecutive PL excitation and emission correlation map. (e) The comparison of the PL emission spectra of the bulk and microscale crystals. (f) Excitation power density dependent PL emission intensity. (g) Temperature-dependent emission spectra. (h) Integrated PL intensity as a function of reciprocal temperature. (i) Temperature dependence of FWHM with theoretical fitting.

blue light emission with high PLQY and characterize its optoelectronic properties. Compared with other OIMHs that have poor stability, easy hygroscopicity, low oxidation resistance, and low photoluminescence efficiency, organic–inorganic zinc-based halides are considered as one of the most ideal luminescent materials due to their low-cost, non-toxicity, high stability, and high emission efficiency. To the best of our knowledge, **(F-PPA)ZnBr$_4$** has one of the highest PLQYs currently reported in 0D zinc-based OIMHs with high detection sensitivity toward UV light.

(F-PPA)ZnBr$_4$ crystallizes in the monoclinic $P2_1/c$ space group with $Z = 2$ as determined from the crystal data and structural refinements (Table S1, ESI†). The experimental powder X-ray diffraction (PXRD) pattern of **(F-PPA)ZnBr$_4$** is consistent with the simulated data from single-crystal XRD analysis (Fig. 1a). As shown in Fig. 1b, $[ZnBr_4]^{2-}$ tetrahedra are formed by four Br^- ions coordinated to every Zn^{2+} ion. The space between these 0D isolated tetrahedra are filled by the organic $[F\text{-}PPA]^+$ cations. Moreover, a certain distortion of the $[ZnBr_4]^{2-}$ octahedra can be observed. This observable torsion partially relieves the selection rule, showing potential promise for the generation of highly efficient luminescent properties. Due to the alternating arrangement of inorganic and organic components in the structure of **(F-PPA)ZnBr$_4$**, this zinc-based halide can be viewed as photoactive $[ZnBr_4]^{2-}$ moieties periodically embedded in the wide bandgap organic matrix, where it displays individual photophysical properties as indicated in Fig. 1b. SEM images show that **(F-PPA)ZnBr$_4$** is highly crystalline and has a regular block-shaped morphology. Elemental mapping indicates the homogeneous dispersion of Zn, Br, N, and F on the crystal surface. Overall, this analysis and characterization successfully confirms the formation of the target product **(F-PPA)ZnBr$_4$**.

Photoluminescence (PL) properties of **(F-PPA)ZnBr$_4$** were systematically characterized in the solid state at room temperature. As shown in Fig. 2a, when irradiated by 355 nm UV light, **(F-PPA)ZnBr$_4$** exhibits bright blue-light luminescence and the PL emission spectrum gives a narrow emission with a centered wavelength of 458 nm and full-width at half-maximum (FWHM) of 60 nm under 365 nm UV light irradiation. The emissive wavelength location of **(F-PPA)ZnBr$_4$** can be demonstrated in the Internationale de l'Eclairage (CIE) chromaticity coordinates of (0.136, 0.097), which is located in the blue region (Fig. 2b). Notably, **(F-PPA)ZnBr$_4$** has a narrow emission wavelength and remarkable PLQY of 50.15%, which is one of the highest values in 0D zinc-based organic–inorganic metal halides except for **(CYP)ZnBr4** so far (Fig. 2c).[22] As shown in Fig. 2d, the 3D consecutive PL/PLE correlation map shows only one emission center in the whole UV light excitation spectrum, indicating that the blue emission is caused by the relaxation of an identical excited state.

In order to get better insight into the PL mechanism of **(F-PPA)ZnBr$_4$**, a series of spectroscopy measurements were applied. The PL spectrum of the microcrystal sample is almost identical to that of the bulk crystal sample, indicating that surface defects are not responsible for the emission (Fig. 2e). The linear relationship between PL intensity and excitation power density of **(F-PPA)ZnBr$_4$** also indicates that this emission does not originate from the permanent defects (Fig. 2f and Fig. S1, ESI†). Furthermore, it can be seen from the temperature-dependent PL emission that **(F-PPA)ZnBr$_4$** exhibits a monotonically increasing emission intensity as the temperature decreases, which is attributed to the weakened thermal associated non-radiative recombination in the cooling process (Fig. 2g). Based on the theoretical fitting of temperature dependent emission intensity according to the Arrhenius equation, **(F-PPA)ZnBr$_4$** gives a thermal activation energy (E_a) of 84.92 meV, which is significantly higher than the room-temperature thermal ionization energy of about 26 meV (Fig. 2h).[23] The emission width gradually broadens from 80 K to 300 K due to enhanced

electron–phonon coupling, and the best theoretical fitting gives a Huang–Rhys factor (S) of 37.05, which is significantly higher than that of conventional semiconductor luminous materials such as ZnSe (0.3), CdSe (1), $CsPbBr_3$ (3.223), and others.[24] The calculated E_{LO} of **(F-PPA)ZnBr$_4$** is 9 meV, which is in good agreement with the strong stretching band at 82.6 cm^{-1} in the Raman spectrum (Fig. 2i and Fig. S3, ESI†). This further confirms the strong electron–phonon interaction in the soft crystal structure of **(F-PPA)ZnBr$_4$**. Altogether, the 3D consecutive PL/PLE correlation map, the temperature-dependent PL emission, and the large Stokes shift of **(F-PPA)ZnBr$_4$** demonstrate that the blue light emission can be attributed to the radiative recombination of self-trapped excitons (STEs) *via* electron–phonon coupling, and the detailed photophysical process is depicted in Fig. S4 (ESI†).

A photoconductive device was fabricated by using a single crystal of **(F-PPA)ZnBr$_4$**, and the photoelectric properties of this device were investigated. The current–voltage (I–V) curve of this device under a 365 nm laser is shown in Fig. 3a. The device exhibits both linearity and symmetry, indicating a robust Ohmic contact between **(F-PPA)ZnBr$_4$** and the Au electrode. The optical response of the device depends on the incident wavelength, and the current induced by light with wavelengths below 200 nm is negligible. The photocurrent intensity noticeably increases when the device is exposed to light with a wavelength of 365 nm under a bias voltage of 10 V, as shown in Fig. 3b. Additionally, the photo-response of the device was evaluated as a function of incident light intensity, whereby a linear increase in response with increasing radiation intensity was observed. This intriguing phenomenon, which exclusively occurs within the wavelength range of 570–750 nm, is ascribed to the selective absorption of light and the polarization properties exhibited by **(F-PPA)ZnBr$_4$**. Moreover, the device can be switched on and off over multiple cycles without any noticeable attenuation, highlighting its favorable stability (Fig. 3c). To evaluate the stability and response characteristics of this photodetector, time-resolved photo-response (TRP) measurements were performed under a 10 V bias. The light was periodically toggled on and off to assess the reliability and stability of the photodetector. It is well known that the response time limitations of the semiconductor characterization system introduce some gaps near the rising and falling edges. To overcome this limitation, an oscilloscope was employed to monitor the transient response time of the **(F-PPA)ZnBr$_4$** photodetector. Utilizing 365 nm laser pulses under a bias of 10 V, this photodetector device demonstrates an extremely stable, ultrafast, and repeatable photo-response. As depicted in Fig. 3d, the rise time indicates the time from 10% to 90% of the maximum signal and the decay time indicates the time from 90% to 10% of the maximum signal, and the rise and decay times are 470 μs and 610 μs, respectively. It is worth noting that the **(F-PPA)ZnBr$_4$** single-crystal photodetector exhibits a significantly shorter response time compared to most photodetectors as well as the most rapid rise time. These results confirm the excellent photoelectric stability of **(F-PPA)ZnBr$_4$**.

To gain insights into the underlying fundamental factors affecting the optical properties of **(F-PPA)ZnBr$_4$**, the electronic band structures were investigated. First-principles calculations are performed by using the Vienna *ab initio* simulation package (VASP). As shown in Fig. 4a, the electronic band structures suggest that the CB minimum and VB maximum are located at different points, implying an indirect E_g of 4.05 eV, which is higher than the value measured by UV-Vis spectroscopy (Fig. S12, ESI†). Detailed investigations reveal that the frontier molecular orbitals of **(F-PPA)ZnBr$_4$** exhibit slight dispersion, indicating strong electronic coupling between adjacent $[ZnBr_4]^{2-}$ units and the Fermi level of the calculated crystal is −0.9185 eV (Fig. 4b). As shown in Fig. 4c, the density of states reveals that the top of the valence band (VB) has contributions from the Br-4p states and Zn-3d states, and the bottom of the

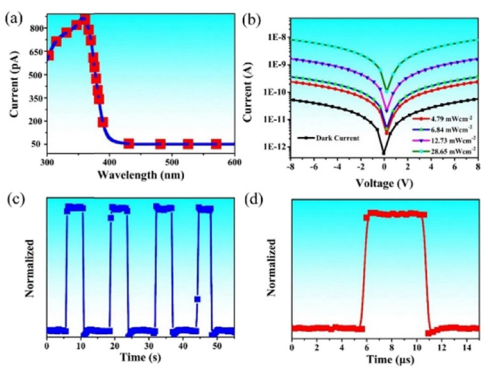

Fig. 3 Visible-blind ultraviolet selective photoelectric response characterization of **(F-PPA)ZnBr$_4$**. (a) Photocurrent-wavelength profile under a bias of 10 V. (b) Photocurrent and dark current measurements under different voltages. (c) Time-dependent switching cycles of photocurrent response. (d) Time-dependent current intensity induced by pulsed-light illumination at 365 nm with a bias of 10 V.

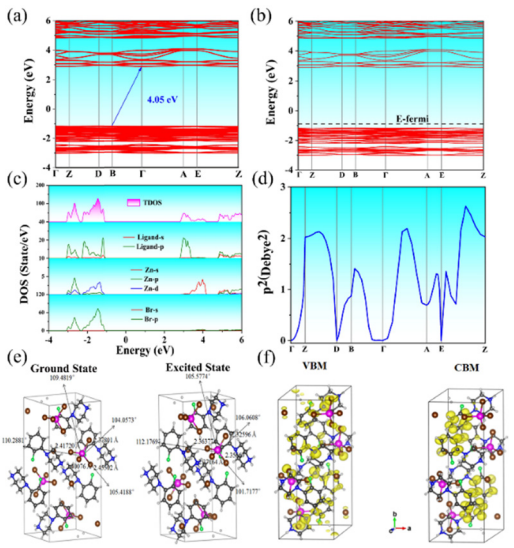

Fig. 4 The theoretical calculation of **(F-PPA)ZnBr$_4$**. (a) Calculated electronic band structure. (b) The density of states (DOS) and partial DOS plots. (c) Fermi level of the calculation. (d) and (e) The calculated excited state and ground state. (f) The highest occupied molecular orbitals and the lowest unoccupied molecular orbitals.

conduction band (CB) is influenced by the Br-4p or Zn-4s states along with the C/N-2p states of the organic cations. This result shows that both the electronic transition within the inorganic component and the inter-electron transition within the organic component in **(F-PPA)$ZnBr_4$** are responsible for its optical properties. Additionally, the transition dipole moment results show that the transition dipole moment of charge at *Z*, *B* and *A* is high, and the transition dipole moment at *Γ*, *D* and *E* is low, which means that the transition is more likely to occur at *Z*, *B*, or *A* (Fig. 4d). The relatively flat nature of the frontier bands in **(F-PPA)$ZnBr_4$** promotes a higher degree of charge localization and enhances the effective masses of both holes and electrons. Notably, all the bands near the Fermi level are extremely flat indicating the highly localized electron states, which promotes the formation of electron and hole polarons indicating the strong quantum confinement in 0D halides. To further unveil the respective contribution of inorganic and organic components, the excited-state geometries of these 0D hybrid zinc halides are optimized. As shown in Fig. 4e and f, the geometries of the organic cations feature negligible change after the photo excitation, while large structural deformations were found in excited-state $[ZnBr_4]^{2-}$ tetrahedrons, demonstrated by the elongated bond lengths and changed bond angles (Table S2, ESI†). The structural deformation degree is associated with the Stokes shift of the PL emission spectra, and the highest value happens in compound **(F-PPA)$ZnBr_4$**. The highest occupied molecular orbital (HOMO) shows that the charge is mainly distributed around the Br atom and the organic ligand, while the lowest unoccupied molecular orbital (LUMO) shows that the charge is mainly distributed around the organic ligand. These results reinforce that the $[ZnBr_4]^{2-}$ tetrahedrons play a vital role in the crystal lattice deformation, giving rise to the formation of STEs.

In summary, a new 0D lead-free metal halide of **(F-PPA)$ZnBr_4$** was successfully characterized and analyzed. This luminescent material exhibits a remarkable combined optical merit of highly efficient blue light emission, high stability and photoresponse selectivity to UV wavelength range. Additionally, combined experimental and theoretical characterizations confirm that the narrowband blue light emission in **(F-PPA)$ZnBr_4$** originates from the intrinsic STE-assisted radiative recombination induced by strong electron–phonon coupling. We believe that this work will provide new guidance for constructing novel 0D lead-free metal halide luminescent materials for optoelectronic applications.

This study is financially supported by the Shandong Provincial Natural Science Foundation Youth Fund (ZR2021QB204), National Nature Science Foundation of China (No. 22201099 and 22171105), Jining University 2019, 2020 ''100 Outstanding Talents'' Support Program Cultivation Project (2020ZYRC02), and the China Scholarship Council (no. 201906650005).

Conflicts of interest

There are no conflicts to declare.

Notes and references

1 Y. Lei, Y. Li, C. Lu, Q. Yan, Y. Wu, F. Babbe, H. Gong, S. Zhang, J. Zhou, R. Wang, R. Zhang, Y. Chen, H. Tsai, Y. Gu, H. Hu, Y. H. Lo, W. Nie, T. Lee, J. Luo, K. Yang, K. I. Jang and S. Xu, *Nature*, 2022, **608**, 317.
2 D. P. McMeekin, P. Holzhey, S. O. Furer, S. P. Harvey, L. T. Schelhas, J. M. Ball, S. Mahesh, S. Seo, N. Hawkins, J. Lu, M. B. Johnston, J. J. Berry, U. Bach and H. J. Snaith, *Nat. Mater.*, 2023, **22**, 73.
3 R. Chakraborty, P. K. Rajput, G. M. Anilkumar, S. Maqbool, R. Das, A. Rahman, P. Mandal and A. Nag, *J. Am. Chem. Soc.*, 2023, **145**, 1378–1388.
4 T. A. S. Doherty, S. Nagane, D. J. Kubicki, Y. K. Jung, D. N. Johnstone, A. N. Iqbal, D. Guo, K. Frohna, M. Danaie, E. M. Tennyson, S. Macpherson, A. Abfalterer, M. Anaya, Y. H. Chiang, P. Crout, F. S. Ruggeri, S. Collins, C. P. Grey, A. Walsh, P. A. Midgley and S. D. Stranks, *Science*, 2021, **374**, 1598.
5 X. Song, G. Wei, J. Sun, C. Peng, J. Yin, X. Zhang, Y. Jiang and H. Fei, *Nat. Catal.*, 2020, **3**, 1027–1033.
6 S. Han, L. Li, C. Ji, X. Liu, G. E. Wang, G. Xu, Z. Sun and J. Luo, *J. Am. Chem. Soc.*, 2023, **145**, 12853–12860.
7 K. Taniguchi, M. Nishio, N. Abe, P. J. Huang, S. Kimura, T. H. Arima and H. Miyasaka, *Angew. Chem., Int. Ed.*, 2021, **60**, 14350–14354.
8 X. Zhang, J. X. Shen, M. E. Turiansky and C. G. Van de Walle, *Nat. Mater.*, 2021, **20**, 971.
9 D. Li, X. Liu, W. Wu, Y. Peng, S. Zhao, L. Li, M. Hong and J. Luo, *Angew. Chem., Int. Ed.*, 2021, **60**, 8415–8418.
10 G. Song, M. Li, Y. Yang, F. Liang, Q. Huang, X. Liu, P. Gong, Z. Xia and Z. Lin, *J. Phys. Chem. Lett.*, 2020, **11**, 1808–1813.
11 J. L. Li, Y. F. Sang, L. J. Xu, H. Y. Lu, J. Y. Wang and Z. N. Chen, *Angew. Chem., Int. Ed.*, 2022, **61**, e202113450.
12 Z. G. Li, M. Zacharias, Y. Zhang, F. Wei, Y. Qin, Y. Q. Yang, L. C. An, F. F. Gao, W. Li, J. Even and X. H. Bu, *ACS Energy Lett.*, 2023, **8**, 3016.
13 B. Li, J. Jin, M. Yin, X. Zhang, M. S. Molokeev, Z. Xia and Y. Xu, *Angew. Chem., Int. Ed.*, 2022, **61**, e202212741.
14 H. Liu, T. B. Shonde, F. Gonzalez, O. J. Olasupo, S. Lee, D. Luong, X. Lin, J. S. R. Vellore Winfred, E. Lochner, I. Fatima, K. Hanson and B. Ma, *Adv. Mater.*, 2023, **35**, 2209417.
15 C. Sun, Z. Deng, Z. Li, Z. Chen, X. Zhang, J. Chen, H. Lu, P. Canepa, R. Chen and L. Mao, *Angew. Chem., Int. Ed.*, 2023, **62**, e202216720.
16 V. Morad, S. Yakunin, B. M. Benin, Y. Shynkarenko, M. J. Grotevent, I. Shorubalko, S. C. Boehme and M. V. Kovalenko, *Adv. Mater.*, 2021, **33**, 2007355.
17 Z. Zhang, Y. Lin, J. Jin, L. Gong, Y. Peng, Y. Song, N. Shen, Z. Wang, K. Du and X. Huang, *Angew. Chem., Int. Ed.*, 2021, **60**, 23373–23379.
18 A. Wang, Y. Guo, Z. Zhou, X. Niu, Y. Wang, F. Muhammad, H. Li, T. Zhang, J. Wang, S. Nie and Z. Deng, *Chem. Sci.*, 2019, **10**, 4573–4579.
19 J. Hu, S. Yang, Z. Zhang, H. Li, C. P. Veeramalai, M. Sulaman, M. I. Saleem, Y. Tang, Y. Jiang, L. Tang and B. Zou, *J. Mater. Sci. Technol.*, 2021, **68**, 216–226.
20 P. Gui, Z. Chen, B. Li, F. Yao, X. Zheng, Q. Lin and G. Fang, *ACS Photonics*, 2018, **5**, 2113–2119.
21 H. Zhou, Z. Song, C. R. Grice, C. Chen, X. Yang, H. Wang and Y. Yan, *J. Phys. Chem. Lett.*, 2018, **9**, 4714–4719.
22 M. Gong, R. Sakidja, R. Goul, D. Ewing, M. Casper, A. Stramel, A. Elliot and J. Z. Wu, *ACS Nano*, 2019, **13**, 1772–1783.
23 T. Ye, X. Wang, K. Wang, S. Ma, D. Yang, Y. Hou, J. Yoon, K. Wang and S. Priya, *ACS Energy Lett.*, 2021, **6**, 1480–1489.
24 X. Cheng, R. Li, W. Zheng, D. Tu, X. Shang, Z. Gong, J. Xu, S. Han and X. Chen, *Adv. Opt. Mater.*, 2021, **9**, 2101975.